RESEARCH

A sensorized wheel coated by solid piezoelectric elastomer

Lorenzo Nicolini[1] · **Davide Castagnetti**[1]

Received: 9 July 2024 / Revised: 10 December 2025 / Accepted: 15 January 2026

Abstract Acquiring mechanical information about the state and the mechanical conditions of wheels, rollers or tyres in real-time working conditions is still a significant challenge in transportation and industrial applications. Non-real-time tests represent the most prevalent method for gathering data about rolling element conditions such as applied load, internal strain and stresses. This study proposes a novel solution to sensorize solid wheels, introducing the use of an innovative piezoelectric elastomer already developed and tested by the authors. Its main characteristics, such as softness and intrinsic sensing capability, make it a good candidate for this type of application. We adapted the fabrication process of the elastomer to the realization of a solid wheel coating, through an ambient temperature over moulding process. A custom dedicated testbench was designed and fabricated to test the prototype wheel under rolling at constant vertical load conditions, in a matrix of different test configurations. Results show that output signals are strongly dependent on load, but also on the velocity due to the system design. A juxtaposed FE analysis integrates test results relating the output voltage signals obtained to the mechanical stress condition of the studied wheel.

Keywords Sensorized wheel · Piezoelectric tyre · Rolling sensor

1 Introduction

Acquiring information from rolling elements, such as wheels or rollers, remains a significant challenge in the current context. In both transportation and industrial applications, tyres and treads play a crucial role in ensuring safety, stability, and performance. Consequently, estimating the forces[1–5] they experience is of utmost importance. Yet, obtaining complex data like vertical load and contact area pressure remains a challenge. Presently, expensive non-real-time tests represent the most prevalent method for gathering data on tread functionality. Researchers have explored various solutions to enhance the understanding of tyre conditions during actual usage. These solutions involve external passive sensor networks integrated into wheels or tyres [6–8]. Moreover, some of the proposed solutions are also useful for energy harvesting purposes, able to energetically autonomize those systems and, in some cases, even able to power other small active sensors [7–11]. However, many of these systems are complex, costly, and necessitate wired networks. Attaining comprehensive data demands significant discretization of the active area of the wheel and, thus, the placement of multiple sensors in different locations. Furthermore, these methods lack scalability for smaller or irregularly shaped wheels. Traditional piezoelectric sensors are typically fragile, rigid, and come in standard flat shapes, making them expensive and difficult to embed.

Meccanica (2026) 61:28 https://doi.org/10.1007/s11012-026-02089-4

Moreover, they are susceptible to damage, thus it is challenging to obtain satisfactory information, particularly from irregular or small wheels.

One interesting approach could involve utilizing a tire material that inherently works as a sensor and exhibits piezoelectric properties. The use of PVDF (Polyvinylidene Difluoride) materials has become widespread in applications requiring high strain and elasticity. However, PVDF remains excessively rigid for numerous applications and is unsuitable for tyre use [12–15]. To address this limitation, researchers have explored different methods and novel materials to create highly flexible and stretchable devices [16–34]. Many of these solutions primarily feature flat or thin elements that can be integrated into other components or used as standalone units. Nevertheless, specific applications, such as the one described here, necessitate the integration of thick and compliant piezoelectric materials tailored to various tyre geometries. Only a few fabrication methods have been developed to produce such tailored soft piezoelectric sensors [35, 36]. Consequently, in this context, the authors previously proposed, studied, developed, and manufactured a new soft piezoelectric elastomer material [37]. This material serves as both a robust, hyper-elastic, and stretchable elastomer and an intrinsic sensor due to its inherent piezoelectric properties. This material has been obtained by mixing an ambient temperature polymerizable bi-component silicone with a piezoelectric ceramic powder, creating a viscous, but liquid solution. A further casting and polarization process has been provided to confer piezoelectric properties and shape to the final artifact. Its adaptable fabrication process is suitable for creating custom shapes and thick elements tailored to specific requirements.

The aim of this study is to demonstrate the applicability of this piezoelectric elastomer [37] to a solid wheel, as those for industrial trucks, which typically feature a metallic hub, coated by an elastomeric polyurethane layer, for damping and grip reasons. This allows for obtaining a coating which has intrinsic sensing capabilities, uniformly distributed on the whole coating volume and all along the circumferential direction. Compared to the classical solutions of a discrete piezoelectric patch integrated in the wheel, this allows the continuous monitoring of the applied load and rotation speed [37]. The proposed wheel has a scalable configuration composed of a metallic hub coated with the soft piezoelectric elastomer, carefully adapted for this case study. Hence, both the required mechanical and piezoelectric properties of the coating are intrinsically combined in an unwired and continuous active compound involving a quick standardizable fabrication process, instead of having discretized sensors carefully wired. The strong suitability of the proposed method extends the possibility to sensorize multiple wheels of different sizes and geometries, adapting the external coating properties. The present study proposes one applicative example carefully tailored to our testing instruments and manufacturing equipment.

The soft piezopolymer, which is radially polarized, is composed of a solution of polymerizable silicone and a ceramic piezoelectric $BaTiO_3$ (*Barium Titanate*) powder [38].

Our project focuses on designing and prototyping the coated wheel, then testing it both experimentally and through static finite element simulation. An analytical model, able to predict the output voltage response of the wheel, was formulated and proposed. We captured the voltage signal using a conductive metallic hub and external laminae positioned on the rolling plane. By analysing these signals, we were able to gather data on the wheel's position, velocity, and the intensity of the vertical load it experienced while rolling.

The experimental results proved the good functionality of the device: the piezoelectric elastomer provides an electric potential difference between the inner and outer faces when rolling under the vertical load and this signal was monotonically increasing with the vertical load applied and with the tangential velocity. From the results we tracked and outlined a function which relates the strain of the elastomer through the thickness direction and the average speed, to the electric output voltage. These two variables are easily decouplable since velocity can be simply measured through the traditional tachymetric approach.

In addition to the intrinsic sensor capabilities of the material, this work proves the simplicity and adaptability of the fabrication procedure. It shows the possibility of achieving free, bulky, tailored shapes, as already claimed in previous work. Good piezoelectric properties make this material able to provide electric voltage under strain, in combination with hyper-elastic response, extremely low elastic modulus and hardness: this makes it suitable for solid tyre applications under low or medium load as in some industrial environments. Although our method is limited to a well-defined material composition, the use of different polymerizable elastomers and piezoelectric powders may be considered to achieve higher piezoelectric performances and different mechanical characteristics of the compound. This study provides a solution to be applied in industrial trucks' wheels, which are currently equipped with solid cast tyres, or where soft rolling elements are involved.

2 Method

2.1 Background and materials

A previous work from the authors [37] presents the piezopolymer used in this work. The mixture is composed of a matrix of polymerizable bi-component silicone *Sylgard 184* [39], whose phase shifts from liquid to solid through the polymerization process, and a particle inclusion of $BaTiO_3$ in powder form [38]. The polymerization starts after the two *Sylgard 184* components (silicone base and reagent) are blended, and it takes from 20 to 30 h to complete the reaction at ambient temperature. The $BaTiO_3$ particle size declared is less than 3 µm but the medium size that was detected by *SEM* (*Scanning Electron Microscope*) inspection (performed with *Nova NanoSEM 450*) settles around 1 µm with a limited variance. According to Chen et al.'s study [40], this grain size maximizes the piezoelectric coefficients.

Since the mixture is initially liquid, it can be cast into the desired shape and polarized simultaneously with the polymerization. The liquid phase of the mixture allows for orienting and aligning particles with a low electric field. At the end of the process, the solution is solid, and all the particles are aligned and stuck into the elastomeric matrix.

According to the previous study, the optimal mixture for the piezoelectric elastomer is characterized by a 50% weight powder concentration and the polarization electric voltage is 1 kV for a unit millimetre thickness. In particular, the chosen parameters come from both the good piezoelectric properties expected and the robustness of the properties at different stress conditions of the material.

2.2 Conceptual design and model definition

The conceptual design in Fig. 1 considers a cylindrical wheel composed of two parts: the inner metallic wheel hub (a in Fig. 1) and the outer solid thick piezo-elastomeric coating (b in Fig. 1). The wheel, loaded by a vertical load P, rolls with angular speed ω, leading to a tangential velocity v over a horizontal plane (c in Fig. 1), including several separated metallic laminae recessed into it, which act as electric contacts.

The load, applied on the hub (P in Fig. 1), deforms the region of the piezo-elastomeric coating around the contact area (brown region in Fig. 1), thus originating an electric potential difference between the inner and outer

Fig. 1 Conceptual model of the rolling wheel under vertical load

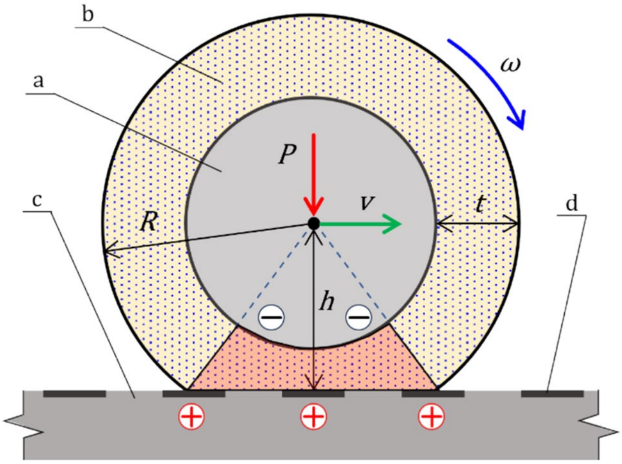

coating surfaces. Thanks to the internal metallic hub of the wheel on one side, and the metallic laminae on the platform on the other side (d in Fig. 1), it is possible to collect and externally transmit this electric signal. Generally, in a closed loop circuit, the electric signal of a piezoelectric device, which is statically deformed, does not persist over time, since it quickly gets neutralized by a discharge phenomenon. In this case, due to the rolling condition, the material under the contact region always changes, new contacts are involved, and thus, a continuous electric generation occurs.

Disregarding the vertical displacement due to load, and assuming an ideal pure rolling condition of the wheel the system is characterized by one degree of freedom.

To allow a simple manufacturing and easy testing of the wheel with the test machine of our laboratory, we chose a radius R equal to 15 mm (Fig. 1), and an axial length of the wheel equal to 30 mm, which ensures a considerable bearing surface considering low vertical loads. The thickness t of the coating layer (Fig. 1) was equal to 25% of the wheel radius (i.e. 5 mm). This value has been selected for the following reasons: first, considering the dimensions of our testing machine, we limited the external wheel diameter to 40 mm. Second, in order to introduce a compliant behaviour of the wheel, thus capable of damping forces when rolling under load, the choice of the thickness considered the low elastic modulus of the elastomeric coating, leading us to choose a value not less than 25% of the wheel radius. Third, on the other hand, a higher thickness requires higher voltages to be poled. This reason limited our absolute value of tread thickness to 8 mm. Lastly, constant and homogeneous poling electric fields can be obtained only if the thin wall condition is satisfied: the electric field of a coaxial cylinder decays hyperbolically as radius increases, leading us to have a R_{ext}/R_{hub} ratio close to 1. In order to achieve a more constant electric field possible during the poling process, we chose the hub radius equal to 15 mm; otherwise, the electric field variation would have led to a weakly poled external surface.

2.3 Prototype fabrication

The fabrication procedure is similar to the process already implemented in the previous study [37]. It consists of the mould design and fabrication, in the casting and curing process.

Considering that the polymeric coating is mainly deformed in the radial direction, we decided to polarize the piezoelectric solution in this same direction. The radial polarization allows the device to be more sensitive according to the expected strains: the drawback is the lower electric field at the outer radius.

Since the piezo-elastomer fabrication method requires a casting process, we opted to overmould the piezopolymer coating onto the wheel hub. This choice leads to important advantages. Firstly, the coating is strongly tied to the inner hub, which, secondly, can be used as an internal electrode for the polarization. Moreover, geometric undercuts can be implemented between the hub and the elastomeric coating to introduce geometric constraints to avoid relative slipping between the two and, ultimately, the entire process becomes lean and quick.

2.3.1 Mould definition and electrostatic analysis

The roller configuration polarized radially allows us to opt for an open mould as shown in Fig. 2, which helps to exhaust the air trapped in the mixture. The mould consists of an axisymmetric geometry, where the symmetry axis coincides with the main rotary axis of the wheel. The mould base (a in Fig. 2) is 3D printed using electrically nonconductive ABS (Acrylonitrile butadiene styrene) plastic through a Dimension BST 768 Stratasys [41]. This part represents the external frame which houses two aluminium electrodes, manufactured by turning: the inner electrode is the hub of the roller (b in Fig. 2); the outer one is an annular component (c in Fig. 2), which has an internal draft of 2° to facilitate the extraction operation, whereas the outer side is fitted into the plastic base by interference and does not present any draft. The electrodes are disposed concentrically with a 5 mm radial gap (tread thickness). The inner electrode (wheel hub) is overmoulded during the casting process: specifically, the hub has two external smaller extensions to be mounted onto a fork, a mechanical stop on the bottom of the mould, and two square-section grooves as geometric constraints for the elastomeric

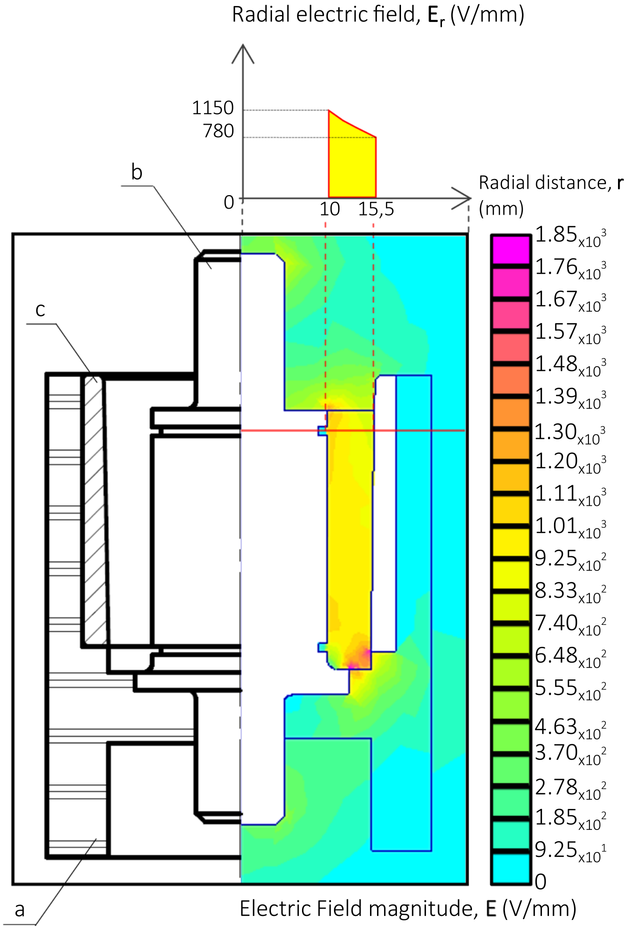

Fig. 2 Section view of the assembled mould: sketch on the left; contour map of the predicted electric field magnitude on the right, with the curve of the radial electric field in the gap between the hub and the outer electrode in the plot on the top

coating. The mould base presents an open hole where to fit one of the wheel hub extensions, allowing also to easily extract the complete cast wheel by pushing it from the bottom after polymerization.

To estimate how homogeneous the electric field is, we implemented an axisymmetric finite element (FE) electrostatic analysis of the radial polarization process through the *FEMM* (*Finite Element Method Magnetics*) [42] software. We applied a triangular mesh and an external area of air approximately three times larger than the zone of interest. Despite the introduced draft on the outer annular electrode, the results confirm that the electric field is circumferentially uniform and sufficiently strong to polarize the material, as shown in Fig. 2. Figure 2 also shows that a small part of the cavity is not enclosed in the high field region: this is due to the fact that the external electrode is shorter than the entire tread length, in order to avoid breakdown phenomena or undesired currents during the curing process. Since both electrodes present sharp edges where electric field intensifications occur, positioning them at different heights increases the distance between two electric field spikes, thus avoiding possible breakdowns. However, there is still an electric field intensification located at the bottom of the cavity, as visible in the contour map in Fig. 2. The electric field in the cavity is circumferentially uniform, but radially it exhibits a hyperbolic variation reported by the plot above, increasing from outside to inside. To avoid breakdowns, the liquid compound helps introduce an insulating barrier, preventing electric discharges between the electrodes. Hence, the cavity must be filled completely. In addition, the mixture must be prepared carefully, checking the absence of air bubbles trapped in the liquid, which may cause unexpected failures in the insulating barrier of the solution. The outgassing process, described below, is crucial. The use of different elastomeric matrices with higher insulating properties could withstand higher electric fields imposed, possibly obtaining higher piezoelectric performances.

2.3.2 Procedure of fabrication

In accordance with the procedure presented in the previous work [37], the fabrication consists in a sequence of steps described below.

- Mixture preparation

The silicone base and the piezoelectric powder, respectively depicted in Fig. 3a and b, are mixed into a bowl in the prescribed ratio using a mixer, until the solution appears uniform. At last, the silicone reagent was added and mixed to start the chemical polymerization reaction. The mixture is shown in Fig. 3c.

- Casting and outgassing process

Since the viscous solution entraps undesired air during the mixing process, it is necessary to remove all the bubbles in order to obtain a final elastomer without air inclusions. To complete this task, we inserted the bowl with the solution in a vacuum chamber (Fig. 3d), connected to an air compressor through a Venturi valve. The reached relative pressure was set at −0.88 bar for 10 min, which ensures a correct degassing. Subsequently, we filled up the cavity pouring the solution from the top opening, and we repeated the outgassing process a second time, ensuring to extract all the air that may have entered during the casting.

- Curing process and extraction

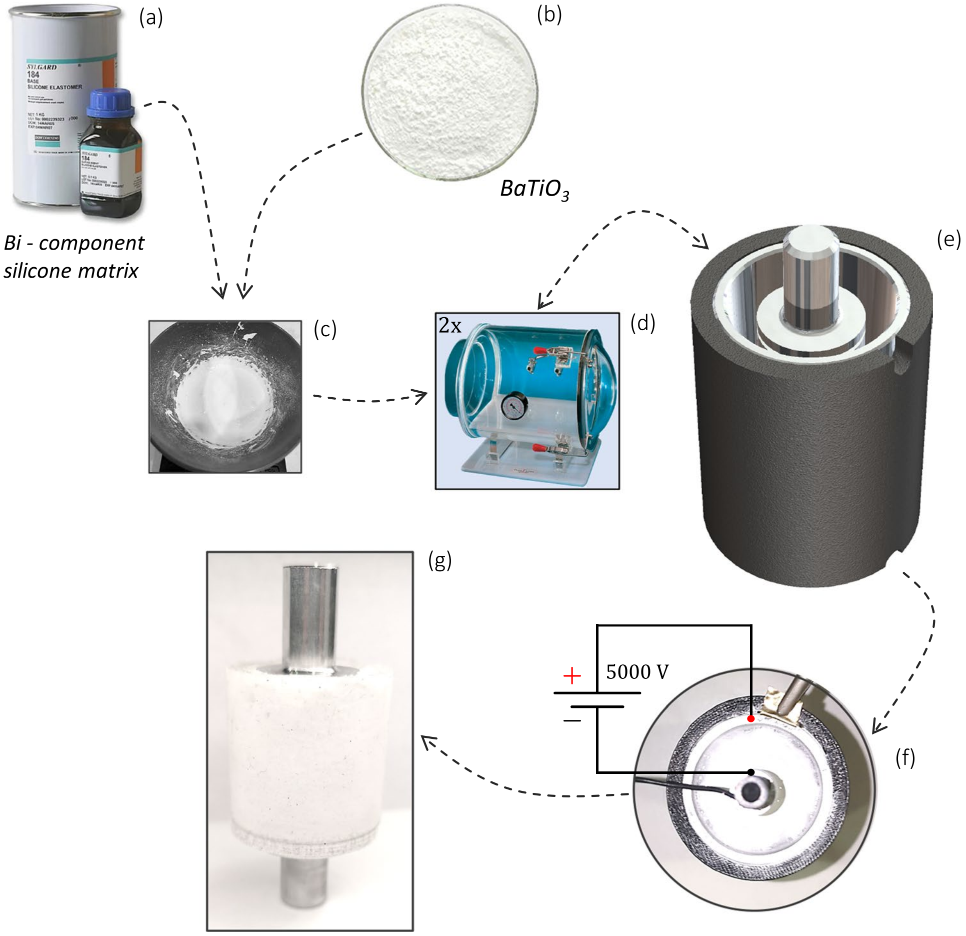

Fig. 3 Fabrication procedure step sequence: **a** Polymerizable bi-component silicone: silicone matrix base *(left)* and reagent *(right)*. **b** Piezoelectric ceramic powder: $BaTiO_3$. **c** Liquid mixture compound. **d** Vacuum chamber for multiple outgassing processes. **e** Rendered perspective view of the whole assembled mould **f**. Real picture of the mould during the curing process: polarization and polymerization. **g** Final sample after the extraction from the mould

The polymerization was combined with the polarization of the liquid solution. The mould's electrodes were connected to a high voltage power supply, which was set to 5 kV in a 5 mm gap. The simultaneous polymerization and polarization lasted for 30 h at ambient temperature (Fig. 3f). After, we extracted the wheel hub with the tied elastomeric coating as Fig. 2g shows.

The piezoelastomeric material used in this research corresponds to the optimal configuration in terms of powder concentration and polarization voltage identified in a previous work by the authors [37]. As shown in the detailed comparison reported therein, this piezopolymer exhibits performances comparable to, or better than, other piezopolymers in the literature, both in terms of ambient temperature Young's modulus and piezoelectric coefficient.

3 Experimental assessment

3.1 Testbench

A custom testbench was purposely designed, built and assembled to test the rolling wheel under load. We applied the load to the fork (a in Fig. 4) in the form of a vertical downward displacement through a servo-hydraulic *MTS Bionix II* testing, at a rate of 1 mm/min [43]. To ensure free rolling of the wheel, the fork supports the wheel axle through a couple of rolling bearings *HK 1012* (SKF). The rolling wheel is loaded against a platform (b in Fig. 4), which is free to translate horizontally since it is supported by three rollers (c in Fig. 4). In the end, each roller is constrained to a base (d in Fig. 4) fixed to the machine frame by a couple of ball bearings *61,900* (SKF), which allows rotation of the roller. The fork, the translating platform and the base were fabricated through *FFF* (*Fused Filament Fabrication*) 3D printing in *Onyx* material. [44] These components were purposely designed to have negligible deformations compared to the wheel's elastomeric coating. However, to ensure the higher accuracy of the investigation, we experimentally measured the stiffness of the sole wheel by performing a quasi-static

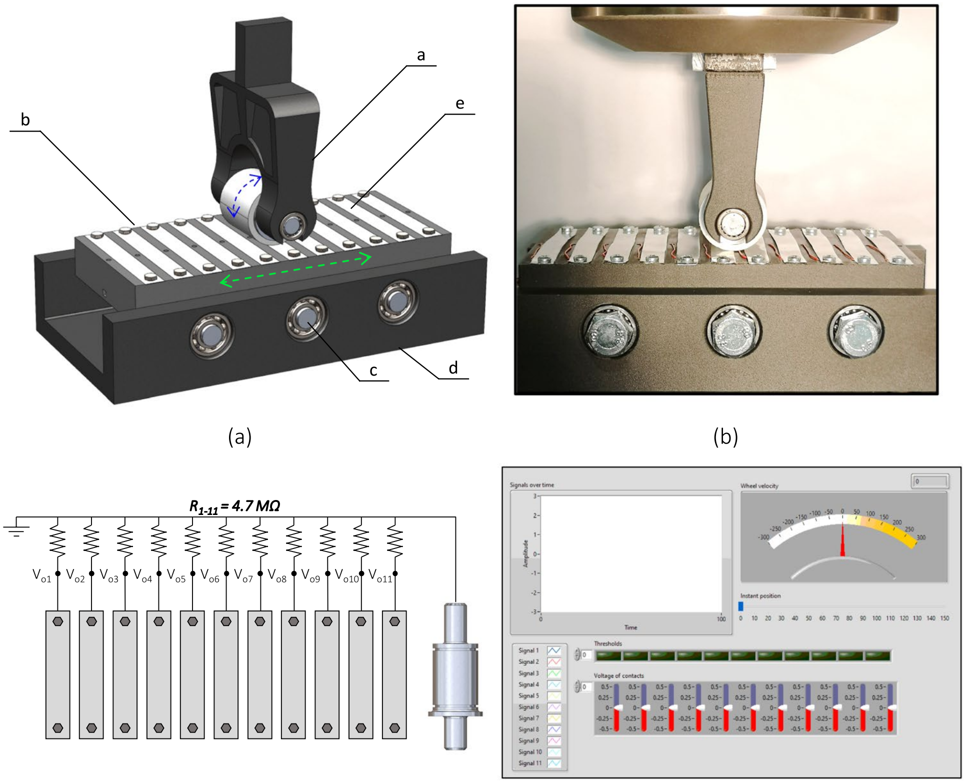

(a) (b)

(c) (d)

Fig. 4 Testbench set up: **a** 3D assembly of instrumentation set up: fork (a), translating rolling plane (b), rotating rollers (c), main fixture mounted onto the tensile machine (d) and separated positive electric contacts (e). **b** Picture of the instrumentation set-up in the testing machine. **c** Representation of the electrical connection, **d** LabVIEW virtual panel for instant data elaboration: virtual plot where signals over time are displayed (top-left), speed gauge (top-right), signal instant vertical bars and position indicator LED (bottom) compression test. This force–displacement curve registered experimentally allowed to removal of the compliance of all the additional components of the system that support the wheel in the tests (fork, axle, bearings, plane, etc.). The translating platform presents a series of eleven equally spaced contacts (e), recessed into the rolling plane in order to have a planar and smooth surface. Each of these contact laminae, which act as the positive terminal of the electric circuit, is fixed on the sides by two screws to the support plate, sufficiently far from the wheel track, while the hub of the wheel acts as the single negative terminal.

A resistive load of 4.7 MΩ was connected in parallel with each contact lamina, according to the schematic in Fig. 4c, and the corresponding electric potential was acquired by a *National Instruments I/O USB-6251* acquisition board [45], connected to a computer equipped with LabVIEW.

As shown in Fig. 4c, in *LabVIEW* [46], we implemented a virtual panel able to register the voltage signals offline and to provide real-time information about the position of the wheel over the rolling plane. Through a plot, the virtual panel showed the real-time intensity of the voltage signals and with an array of eleven vertical bars used as real-time indicators of the acquired voltages, simulated in real time the contact of the wheel with the rolling plane. A corresponding array of LEDs was used to determine the instantaneous wheel position upon reaching a prescribed voltage threshold of 0.1 V. Until another LED turns on, the position is supposed to be the previous one detected and it is shown by a horizontal indicator bar. Finally, the instantaneous velocity is calculated by exploiting the position rate of change, roughly indicated through a dial.

3.2 Test plan

To assess the wheel's piezoelectric performances and characteristics, we performed rolling tests under load. The tests involved four strain levels (0.5, 5, 10, 15 and 20% of the coating thickness) corresponding to a load of 5, 13, 38, 90, and 160 N, respectively. On the one hand, the lowest strain level (0.5%) corresponded to the minimum preload, which ensured the pure rolling condition of the wheel all over the rolling plane. On the other hand, exceeding 20% of vertical deflection would have introduced non-negligible measurement errors because of the testbench compliance. While the force was kept constant during each test, the rolling plane was manually translated ten times from one end to the other, at three different speeds. Due to the manual process and the shortness of the translating platform, we were not able to ensure a precise and constant speed along the whole path; thus, we considered ranges of velocity highly different from each other: 90–110, 170–210, 300–350 mm/s.

It comes an experimental assessment characterized by a matrix of 15 configurations: the voltage signals were acquired simultaneously by the eleven contacts and recorded at a sampling time of 1000 Hz. For each configuration, we calculated the maximum voltage value that occurred and the average voltage value, only including those values for which the position of the wheel on the relative contacts was verified at that instant of time (space–time correspondence).

4 Analytical study

This section aims to describe the physical wheel response through an analytic approach combined with a numerical electrostatic model: the result is a predictive voltage equation function of the vertical deflection, position, and velocity. The numerical model helped us to carefully estimate the electric capacitance of the wheel over a flat plate, in different conditions of vertical deflection and horizontal relative position between the two. From the numerical results, we derived an analytic electric capacitance law, which is a basis for the analytical model. The model relies on the following assumptions: first, we neglected the draft angle, considering the wheel coating as a perfect cylinder. Secondly, we considered the piezoelectric coating as a homogeneous compound all over the coated surface, both in terms of mechanical and piezoelectric properties. Third, we focused on a single flat contact lamina where the wheel rolls over. Fourth, only radial displacement has been considered to contribute to the electric signal. Figure 5a describes the front view of the wheel: to calculate the amount of electric charge Q deployed

Fig. 5 Analytical–numerical study:**a** scheme for analytical study depicting a flattened wheel and reporting important variables including the active width of contact and the total region radially deformed (hatched region); **b** Equivalent electric circuit of the piezoelectric coupling and the external circuit introduced; **c** Electrostatic 3D finite element analysis of the wheel over a single flat contact in centred position, shifted by 7.5 mm and 15 mm: mesh and results in terms of electric potential and electric capacitance of the electrostatic coupling between the wheel and the flat contact; **d** surface interpolation (red net) of the capacitance values obtained in the FE analysis (black hollow circles). (Color figure online)

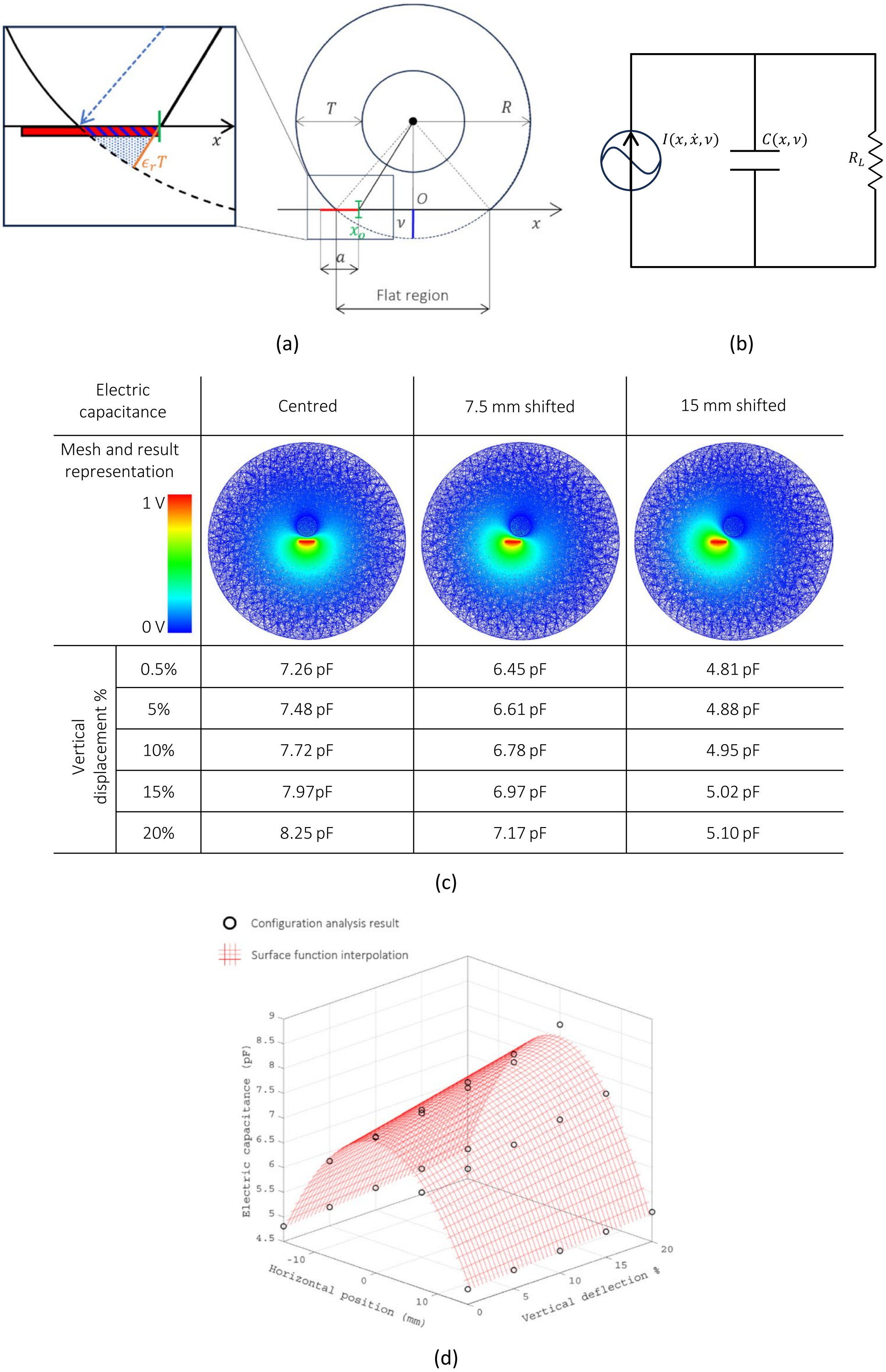

Electric capacitance		Centred	7.5 mm shifted	15 mm shifted
Mesh and result representation				
Vertical displacement %	0.5%	7.26 pF	6.45 pF	4.81 pF
	5%	7.48 pF	6.61 pF	4.88 pF
	10%	7.72 pF	6.78 pF	4.95 pF
	15%	7.97pF	6.97 pF	5.02 pF
	20%	8.25 pF	7.17 pF	5.10 pF

by the piezoelectric coating, we integrated its radial strain ϵ_r occurred over the flat contact area A and multiplied it by the induced polarization coefficient d_r over the elastic compliance s_r, which gives the following equation:

$$Q(x, v) = \frac{d_r}{s_r} \int_A \varepsilon_r dA\prime = \frac{d_r}{s_r} b \int_{x-k}^{x} \left(\frac{R}{T} - \frac{\sqrt{(R-v)^2 + x\prime^2}}{T} \right) dx\prime \tag{1}$$

Hence, the electric current I provided by the piezoelectric coating can be calculated by deriving the charge $Q(x, v)$ in respect to time, thus obtaining:

$$I(x, \dot{x}, v) = \frac{d(Q(x, v))}{dt} = \frac{d_r}{s_r} b \cdot \frac{d}{dt} \left(\int_{x-k}^{x} \left(\frac{R}{T} - \frac{\sqrt{(R-v)^2 + x\prime^2}}{T} \right) dx\prime \right) \tag{2}$$

where:

$$k = \begin{cases} a, a - \sqrt{2Rv - v^2} < x < \sqrt{2Rv - v^2} \\ x - \sqrt{2Rv - v^2}, x \geq \sqrt{2Rv - v^2} \\ -x - \sqrt{2Rv - v^2}, -\sqrt{2Rv - v^2} \leq x \leq a - \sqrt{2Rv - v^2} \end{cases} \tag{3}$$

Specifically, d_r is the induced polarization piezoelectric coefficient, in case both stress and charge density are radially oriented; s_r represents the radial mechanical compliance of the elastomer, ε_r is the local radial strain, and A is the total area in contact with the lamina. With regard to Fig. 5a, the term b represents the depth of the cylinder, v is the vertical deflection imposed and x is the relative horizontal position of the right edge of the lamina with respect to the wheel centre. Moreover, a represents the lamina's width and k is an integration parameter dependent upon position. T and R are respectively the thickness of the coating and the radius of the wheel.

Once we defined the electric current function I, we represented the electric circuit and the piezoelectric interaction of rolling wheel with a Norton's equivalent circuit as reported by Park [47], since it suits perfectly with our mathematical model. Figure 5.b shows the circuit representation, which corresponds to the following output voltage function:

$$V_o(t) = e^{-(R_L^{-1} \int C^{-1}(x,v)dt)} \cdot \left(c_1 + \int \frac{I(x, \dot{x}, v)}{C(x, v)} e^{(R_L^{-1} \int C^{-1}(x,v)dt)} dt \right) \tag{4}$$

where V_o is the output voltage signal, R_L represents the load resistance applied, C is the electric capacitance originated by the piezoelectric element interposed between the two contacts (wheel hub and a contact lamina) c_1 is the integration constant.

As reported in Eq. 4, the electric capacitance is a function of the vertical deflection v and the horizontal relative position x. As mentioned above, it is not accurately achievable from an analytical study; therefore, we decided to obtain it from a numerical electrostatic 3D FE model, implemented through the Elmersolver in the FreeCAD environment [48, 49]. As reported in Fig. 5c, we investigated the effects of two variables: horizontal position (over three levels) and vertical deflection (over five levels), giving a full factorial numerical test plan of 15 configurations. Figure 5c shows the contour map of the electric capacitance for three different levels of the horizontal displacement. The model includes the wheel hub and the flat contact centred in a spherical region of air, which defines the analysis's domain. The mesh is composed of tetrahedral elements which present a characteristic side length set to 1 mm in the sphere centre, whereas increasing up to 10 mm by the external sphere surface. We applied a unitary voltage jump between the flat contact and the wheel's hub, which has the same potential as the far-field equal to zero at the outer boundary. For each configuration, the model describes the wheel coating with its real deformed geometry as a consequence of the vertical displacement applied. In order to calculate the electric capacitance, C, we included the relative dielectric permittivity of the piezoelectric coating $\epsilon_r = 4.78$, deriving it from previous study's measurements [37, 50], which effectively enhances the overall capacitance.

By fitting the values obtained from the above multiconfiguration analysis, we outlined the following surface function:

Table 1 Coefficients of the interpolating electric capacitance function

a (pF/mm^2)	b (pF/mm)	c (pF/mm^3)	d (pF)
$-1.03 \cdot 10^{-2}$	$4.62 \cdot 10^{-2}$	$1.04 \cdot 10^{-4}$	7.11

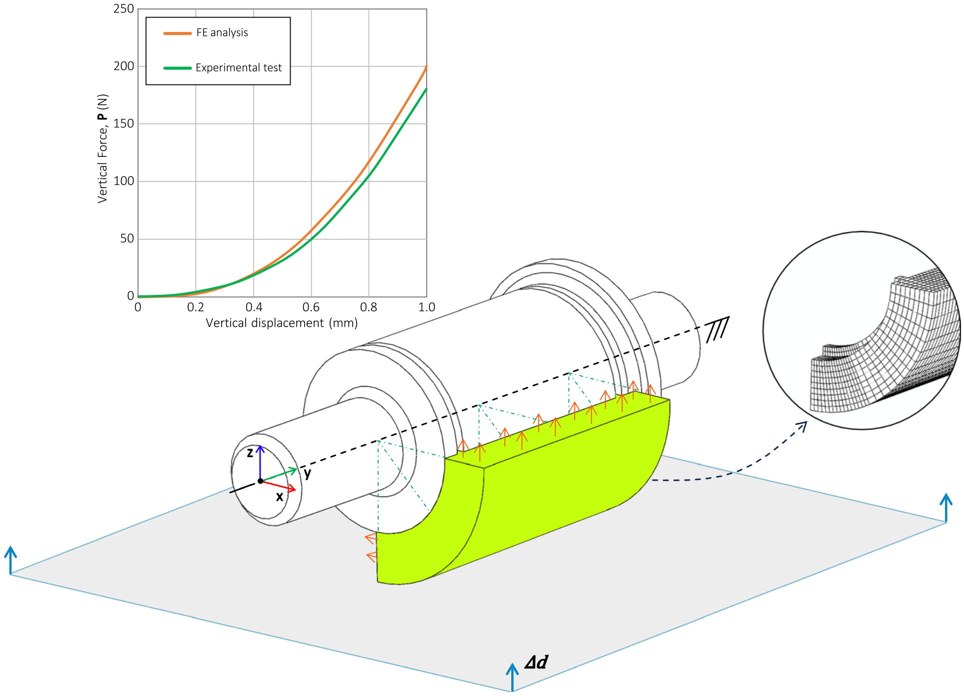

Fig. 6 FE analysis: problem definition, constraints, mesh, and force–displacement comparison with real experimental test

$$C(x, v) = ax^2 + \left(b - cx^2\right)v + d \tag{5}$$

where a, b, c and d are the fitting coefficients ($R^2 = 0.99$) reported in Table 1. A plot of the surface function is reported in Fig. 5d.

5 Finite element analysis

To compare the test results, have a better and complete understanding of the load state and a prediction tool of the system response, we implemented a geometrically non-linear 3D FE analysis that estimates the contact footprints and the contact pressures at different levels of deformation. The model, implemented through the commercial software *Abaqus 6.20*, only describes the quasi-static compression of the wheel, while neglecting the piezoelectric response, and was carefully calibrated with the experimental data.

Thanks to the vertical and horizontal symmetry planes (y–z and x–y, respectively, in Fig. 6), the 3D FE model describes only a quarter of the elastomeric coating of the wheel (see Fig. 6), as a solid body: the effect of the rigid internal hub (not represented) on the elastomeric coating was modelled by applying a kinematic coupling constraint [51] between the nodes lying on the inner surface of the coating and the reference control point placed along the wheel axis. Hence, the internal face nodes are rigidly connected to each other and fixed to their reference control point placed along the main axis. In addition, the model describes the rolling plane by an analytical rigid surface, identified through a reference point. The mesh applies hexahedral quadratic *C3D20R* reduced integration elements, and it is divided in two regions along the circumferential direction (Fig. 6): the first includes the region in the area of contact, with an average element side length equal to 0.4 mm; the second uses a coarser mesh (side length close to 1.2 mm) but includes mesh transition toward the contact area region to increase the accuracy. The model implemented a hyper-elastic material model with the stress–strain curve calculated in the previous work by the authors [37]: specifically, the Young's modulus and the Bulk modulus of the material were equal to 9 and 75 MPa, respectively. According to Liu's work, which introduced *Sylgard 184* material for the realization of viscoelastic domes [52], we assumed a Poisson's ratio equal to0.48. This means that we assumed a negligible effect of $BaTiO_3$ inclusions on Poisson's ratio and we neglected the piezoelectric response of the material since the test was quasi-static and the system was in an open-circuit configuration. We defined a frictionless "hard contact" interaction [53] between the elastomer and the surface of the rolling plane. The model applies symmetry constraints to the two symmetry planes of the wheel coating (i.e. zero translation in the direction normal to the symmetry plane), and full constraints to the reference point which controls the inner surface of the coating. Thus, to reproduce the experimental tests, the static non-linear simulation applies the same five strain levels in subsequent analysis steps, including preload (Sect. 3.2) by simply applying a vertical upward displacement to the analytical rigid surface.

6 Result and discussion

For each of the prescribed five load levels at the 250 mm/s speed, Fig. 7 illustrates the output voltage signal over time registered by the lamina placed in the middle of the translating platform (b in Fig. 4), when the loaded wheel rolls over it. We report the output voltage on this lamina, since in this position the wheel speed is nearly constant.

Figure 7 shows the typical response of the proposed smart wheel: the voltage signal from the piezoelectric polymer changes its sign from compression to relaxation. These signals are purposely taken directly from measurements without any further filtering operation in order to also provide a direct comparison between signals and noise. During the compression phase, we initially observe a negative voltage, meaning that the coating layer is compressed against the lamina up to reach a negative peak; this peak is followed by an abrupt decrease of the voltage signal, corresponding to the beginning of the unloading phase, up to a positive voltage peak. Then, a positive transient phase of electric discharge restores the zero potential difference. As Fig. 7 shows, the load increase corresponds to an overall higher voltage response and also higher signal irregularity. The latter may be given by noise increments and by a slight variability of piezoelectric properties on the coating surface, due to a possible inhomogeneity of the elastomeric compound. The voltage peak depends not only on the vertical deflection imposed, thus the strain on the coating, but also on the velocity at which the loading and the release phase of the elastomeric coating occur. Whereas the transient of the loading phase depends on the tangential velocity, the release phase depends on the relaxation time of the material and on the vertical deflection imposed. As Fig. 7 shows, at higher loads the voltage signal lasts longer, which can be attributed to the larger contact area of the deformed wheel. At the constant velocity condition, larger contact areas increase the time spent to transit over the laminae, because the wheel gets in touch earlier with it and separates later. Hence, the time spent by the wheel over the lamina is not strictly equal in different load conditions and, since the electric charge drops with a rate dependent on the equivalent circuit characteristic, this slightly affects the voltage peak value reached, depicting a complex relation among vertical load or vertical deflection, tangential velocity, and the maximum voltage peak.

For all the configurations investigated, Fig. 8 shows the average values of the voltage response from the wheel, as a function of its tangential velocity and the vertical load applied. Each curve refers to a range of velocity and the points represented by the hollow circles correspond to the average of the voltage values registered on the laminae during the wheel transition for that given speed. To calculate average voltage values, we only considered the positive part of the curve (see curves in Fig. 7). For each configuration, contact pressure and vertical displacement contour maps predicted by FE are included, and relative contact area and flattening angle are reported.

As shown in Fig. 8, regardless of the speed of the wheel, the output voltage significantly increases with the vertical strain level: since the lowest value of strain (0.5%), the wheel exhibits a significant response in

Fig. 7 Output voltage signal over the lamina placed in the middle of the platform (b in Fig. 4) at 0.5% **a** 5% **b** 10% **c** 15% **d** 20% **e** of vertical imposed displacement

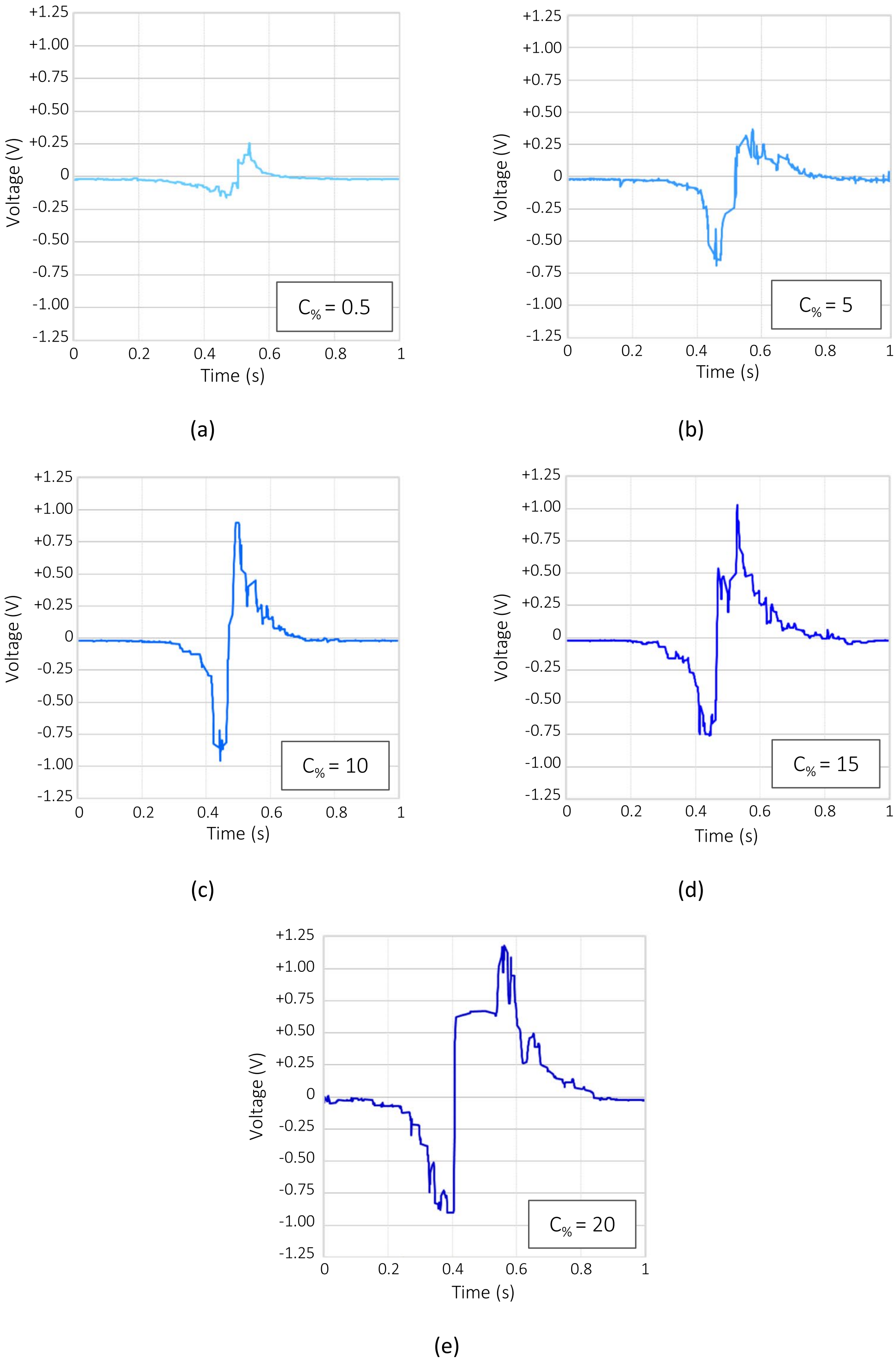

terms of output voltage; this value increases by increasing the vertical displacement applied up to more than 0.75 V at the higher speed. Also, the tangential velocity has a remarkable positive effect on the output from the wheel, with a noticeable difference between the three levels investigated. This behaviour depends on the piezoelectric property of the coating, the total area in contact, and the corresponding local compression strain along the polarization direction (radial direction).

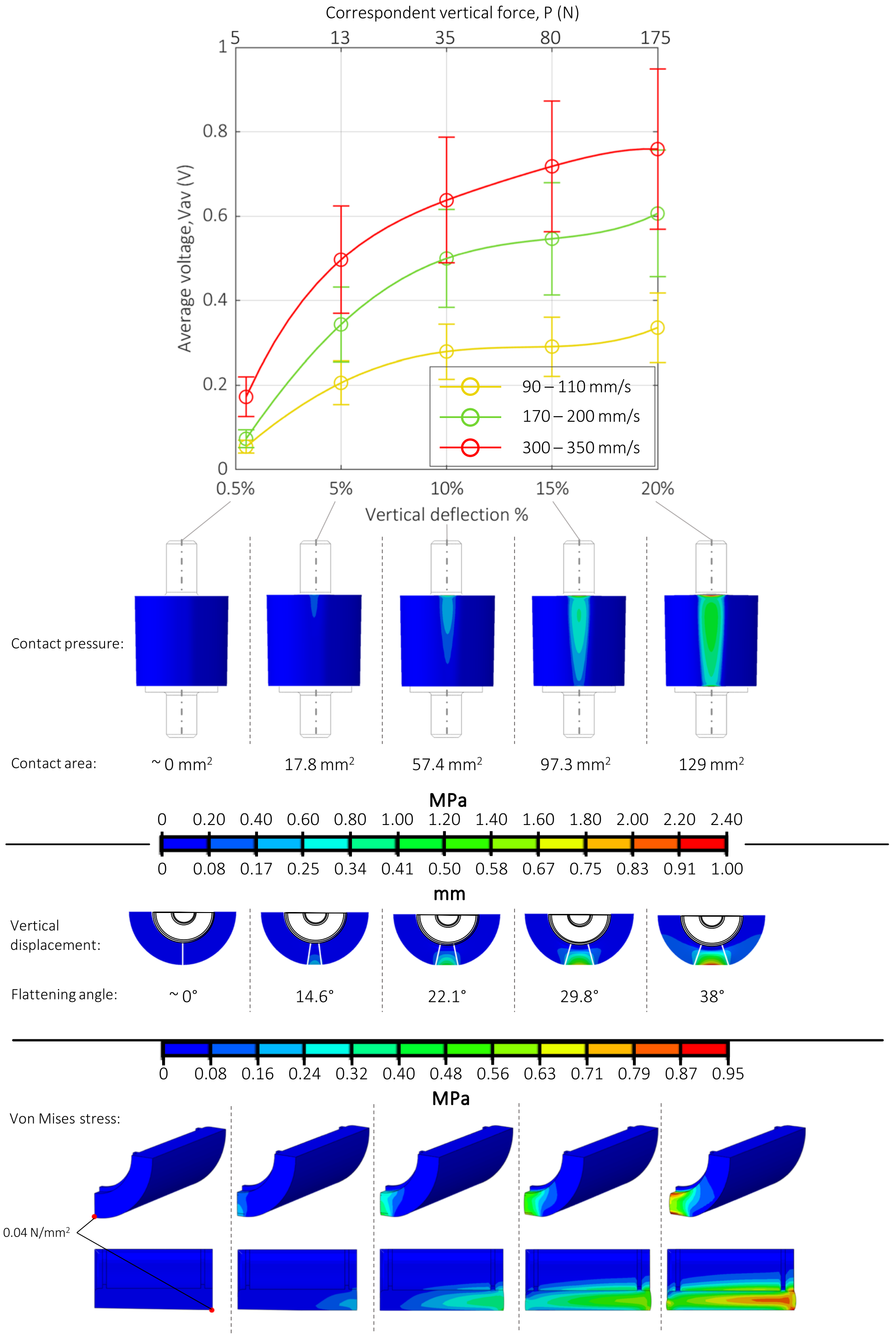

Fig. 8 Plot results of the average voltage signal in the tested configurations and FE results predictions: contact pressure, contact area, vertical displacement, flattening angle and von Mises stresses

Moreover, the tangential velocity defines the strain rate of the elastomeric coating over contacts, thus affecting the amount of time the wheel maintains contact with each lamina. According to the equivalent circuits of piezoceramics proposed by Park [47] and its application in our previous study [37], as studied in Sect. 4, the equivalent electric circuit of the systems includes two main effects: first, the intrinsic capacitor effect originated by the hub and laminae with the piezoelastomer in between, which is described by a variable capacitance term described by Eq. 5 (illustrated in Fig. 5); second, a discrete resistive load equal to 4.7 MΩ, which is added to the circuit to restore the potential difference at zero and reduce the signal noise. The combination of the intrinsic capacitance with the discrete resistive load makes the circuit work like a high-pass filter (HPF). This explains why higher voltage values are achieved when the piezoelectric material flows faster through the contact region. This phenomenon also happens in most commonly used piezoelectric devices because two contacts are needed, and they sandwich the piezoceramic part of the device. In those cases, the faster the impulse, the higher the voltage signal. In our situation, this translates to the rolling speed of the wheel: the faster the wheel rolls, the quicker the impulse becomes. To reduce this strong dependence on speed observed in the experiments, a possible solution is to introduce an additional capacitor in the electric circuit: this could effectively change the electrical response of the circuit.

The FE analysis predicts the contact area, the contact pressure and the local vertical displacement at each load level investigated, for a static condition of the wheel. The comparison between tests and FE analysis allows us to outline a direct relationship between the average voltage signal detected and the inner condition of the wheel coating, estimating in real time loads and stress conditions of the wheel. The flattening angle detects the width of the contact footprint from a side view, here represented by the largest lateral face of the wheel. It has the vertex along the rotary axis and the two half-lines passing through the extremes of the contact area (flat zone). This angle is a size-normalized indicator of how much the wheel is vertically strained, and it is independent of its diameter.

The FE analyses reported here are purely static and do not take into account the (time-dependent) viscoelastic properties of the wheel coating during rolling. This simplifying assumption is fully acceptable at low speed, whereas at high rolling velocity, the intrinsic viscoelastic properties of this material could affect the response. Specifically, viscoelasticity is responsible for an unsymmetric wheel footprint, which could reasonably better explain why signals have different positive and negative charge and discharge durations. To simulate this viscoelastic effect, a Steady State Transport Analysis [54] can be used. This dynamic analysis, specifically tailored for wheels, provides the steady state results of a wheel having time-dependent material properties and involves both Lagrangian and Eulerian meshes. However, this goes beyond the scope of this research.

By interpolating the average voltage values acquired experimentally, we outlined a fitting polynomial function (Eq. 6), which predicts the voltage response of the wheel as a function of tangential speed, v, and percentage vertical strain, $c_{\%}$ of the wheel itself:

$$V_{av}\left(c_{\%}, v\right) = \mathrm{p}_{00} + \mathrm{p}_{10}c_{\%} + \mathrm{p}_{01}v + \mathrm{p}_{20}c_{\%}^{2} + \mathrm{p}_{11}c_{\%}v + \mathrm{p}_{30}c_{\%}^{3} \tag{6}$$

where p_{ij} are the polynomial coefficients, reported in Table 1.

This function accurately fits the acquired data with a coefficient of determination R^2 equal to 0.998. In particular, the polynomial proves the linear response with respect to the wheel tangential velocity and the cubic behaviour with respect to the imposed vertical displacement. The interaction between the two variables also has an influence on the average voltage. When both $c_{\%}$ and v are equal to zero, the system is expected to provide an average voltage equal to zero; thus, the constant term p_{00} should result in null. However, the first column in Table 2 reports a p_{00} different from zero and it may be an indicator of the measurement error, which is sufficiently low to be considered negligible.

The outlined function can be easily decoupled into its two main variables by simply tracking the wheel position over time, detecting where the signal is coming from and at what instant of time. Hence, tangential velocity can be simply obtained without quantitatively analysing the voltage signals. Once the velocity is known, it is easy to obtain the sole vertical displacement voltage contribution. All other minor influencing factors, which may affect the single voltage measurement, are mitigated. Anyway, further improvements on

Table 2 Polynomial coefficients of the interpolating function

p_{00}(V)	p_{10}(V)	p_{01}(V/mm)	p_{20}(V)	p_{11}(V/mm)	p_{30}(V)
$-4.3 \cdot 10^{-3}$	$-2.49 \cdot 10^{-2}$	$1 \cdot 10^{-4}$	$-4 \cdot 10^{-3}$	$4 \cdot 10^{-4}$	$1 \cdot 10^{-4}$

the fabrication process should lead to better repeatability, reducing a possible inhomogeneity which is currently given by a manual fabrication method. Nevertheless, all applications of the proposed study need to be previously tested and calibrated, in order to match the electrical signal with the corresponding compression level, and to verify the signal repeatability on site.

Figure 9 shows the surface fit function.

From Fig. 9 appears that the interpolating surface obtained from Eq. 1 accurately fits the experimental data from the wheel.

The long-term stability of the device has not been deeply investigated. Nevertheless, the several tests at different compression levels performed during the setup of the procedure did not indicate any degradation of the piezoelectric signal. However, under repeated exposure to high compression levels, a slow degradation of the piezoelectric response may be expected, since high strains in the elastomer could progressively induce unalignments of $BaTiO_3$ dipoles embedded in the silicone matrix. From a mechanical perspective, we would expect a strong wear resistance of the piezoelastomeric coating, comparable to that of pure silicone.

The main drawback of the proposed device is the need for a dedicated rolling plane equipped with separated and wired contacts. Nevertheless, wires are fixed and still and no moving wires and electrical connections are present except for the negative connection on the hub. Moreover, the use of this type of rolling plane also allows us to detect the wheel position over it easily. A straightforward development would be to extend the contacts pattern from a row of contacts to a grid in order to detect the position over a two-dimensional space instead of one-dimensional.

The further main development of this work would be extending its functionality to conventional floors or roads, where no contacts or wires are present and cannot be implemented. This possible advancement would be possible only by implementing a second conductor element on the external side of the wheel. Among all possibilities, a reachable and fast feasible solution may involve the use of protected and separated thin metallic sheets, even though possible mechanical drawbacks may bring additional limits. Alternatively, a more challenging yet innovative solution may be introducing a further electrically conductive PDMS/SCF thin coating (based on the same elastomeric matrix) as an external conductor [55], alternating it with a traditional PDMS layer. Although this last option may reduce the signal amplitude because of the higher resistivity compared to metals, it would provide a similar mechanical response. The main challenge is embedding the external, separated contact wires within the elastomeric coating to achieve a solid-state and compact sensing device.

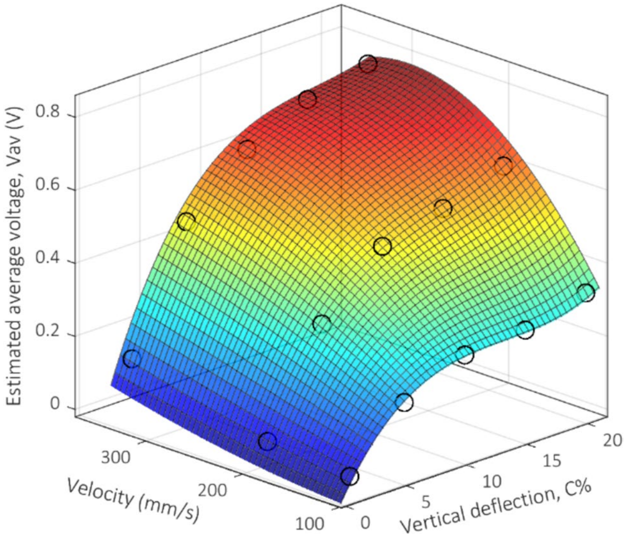

Fig. 9 Surface Fit function reporting average voltage achieved over vertical load and rolling velocity

7 Conclusions

This study proves the applicability of the already developed piezoelectric elastomer as an external active and solid coating for scalable and geometrically varied wheels. The aim of this study is to introduce a new way to sensorize wheels by introducing the use of this innovative piezoelectric elastomer with sensing capabilities, unitedly with its own flexible fabrication process. This work adapts the piezo elastomer casting procedure to an over-moulding of a wheel hub. This piezo elastomer presents all the main features required for this type of application, such as softness and intrinsic piezoelectricity to confer, respectively, compliance and sensing capabilities. A custom testbench made of a sliding platform with multiple separated contacts and a fork was appropriately designed and fabricated to test the wheel under constant vertical load and during rolling conditions, acquiring the voltage signals. The external coating provides a transient electric potential difference when deformed between the inner hub and the sliding floor. Test results provided the average voltage signal values at different tangential velocities of the wheel and at different vertical loads applied. A strong and direct dependence on vertical load and velocity was detected, and a response surface function, which on average predicts the voltage response of the wheel, has been outlined. A juxtaposed FE analysis integrates all the results not directly achievable from the tests. The FE results integration allowed us to directly relate inner wheel conditions to the average voltage signal produced in real time. Finally, the piezoelectric intrinsic characteristic of the wheel coating proposed allows for sensorizing small, irregular, or geometrically varied wheels, avoiding a high number of sensors, offering new developable solutions partly listed in this work. The use of different piezoelectric powders and elastomeric matrices has yet to be proved, but it may lead to other possible solutions to achieve different stiffnesses, hardnesses, and electrical responses of the compound.

8 Conflict of interest

The authors declare no competing interests.

Author Contribution Lorenzo Nicolini: Conceptualization, Methodology, Software, Validation, Formal analysis, Investigation, Resources, Data curation, Writing – original draft, Visualization, Project administration. Davide Castagnetti: Conceptualization, Resources, Writing – original draft, Writing – review & editing, Supervision, Funding acquisition.

Funding Open access funding provided by Università degli Studi di Modena e Reggio Emilia within the CRUI-CARE Agreement.

Data Availability No datasets were generated or analysed during the current study.

References

1. Castagnetti D, Dragoni E, Mammano GS (2008) Elastostatic contact model of rubber-coated truck wheels loaded to the ground. Proc Instit Mech Eng, Part L: J Mater: Des Appl 222(4):245–257. https://doi.org/10.1243/14644207JMDA185

2. Longoria RG, Brushaber R, Simms A (2019) An in-wheel sensor for monitoring tire-terrain interaction: development and laboratory testing. J Terramech 82:43–52. https://doi.org/10.1016/j.jterra.2018.12.004
3. Jittham P, Sucharitpwatskul S, Siriruk S, Meesaringkarn S (2022) Finite Element Analysis of elastomer: Case study – Rolling resistances of pneumatic and solid tyres. IOP Conf Ser Mater Sci Eng 1234(1):012002. https://doi.org/10.1088/1757-899X/1234/1/012002
4. Phromjan J, Suvanjumrat C (2018) A suitable constitutive model for solid tire analysis under quasi-static loads using finite element method. Eng J 22(2):141–155. https://doi.org/10.4186/ej.2018.22.2.141
5. Anghelache G, Moisescu A-R, Buretea D (2017) Assessment on the methods of measuring the tyre-road contact patch stresses. IOP Conf Ser Mater Sci Eng 227:012006. https://doi.org/10.1088/1757-899X/227/1/012006
6. Yang S et al (2022) An intelligent tyre system for road condition perception. Int J Pavement Eng. https://doi.org/10.1080/10298436.2022.2096882
7. Kubba A, Jiang K (2014) A comprehensive study on technologies of tyre monitoring systems and possible energy solutions. Sensors 14(6):10306–10345. https://doi.org/10.3390/s140610306
8. Askari H, Hashemi E, Khajepour A, Khamesee MB, Wang ZL (2019) Tire condition monitoring and intelligent tires using nanogenerators based on piezoelectric, electromagnetic, and triboelectric effects. Adv Mater Technol 4(1):1800105. https://doi.org/10.1002/admt.201800105
9. G. Manla, N. M. White, and J. Tudor, (2009) Harvesting energy from vehicle wheels. In: TRANSDUCERS 2009 - 2009 International Solid-State Sensors, Actuators and Microsystems Conference, IEEE, pp 1389–1392 https://doi.org/10.1109/SENSOR.2009.5285831
10. O. J. Jousimaa, Y. Xiong, A. J. Niskanen, and A. J. Tuononen, (2016) Energy harvesting system for intelligent tyre sensors. In: 2016 IEEE Intelligent Vehicles Symposium (IV), IEEE, pp 578–583 https://doi.org/10.1109/IVS.2016.7535445
11. Aditya Pandey, 2020 Energy Generation in Tyres using Piezoelectric Material. Int J Eng Res Technol, 9(7) https://doi.org/10.17577/IJERTV9IS070547
12. Zeng F, Sun Y, Zhou Y, Li Q (2011) A molecular dynamics simulation study to investigate the elastic properties of PVDF and POSS nanocomposites. Model Simul Mater Sci Eng 19(2):025005. https://doi.org/10.1088/0965-0393/19/2/025005
13. Pei Y, Zeng XC (2011) Elastic properties of poly(vinyldene fluoride) (PVDF) crystals: a density functional theory study. J Appl Phys. https://doi.org/10.1063/1.3574653
14. Ahmad Z, Prasad A, Prasad K (2009) A comparative approach to predicting effective dielectric, piezoelectric and elastic properties of PZT/PVDF composites. Physica B 404(20):3637–3644. https://doi.org/10.1016/j.physb.2009.06.009
15. Mullaveettil FN, Dauksevicius R, Wakjira Y (2021) Strength and elastic properties of 3D printed PVDF-based parts for lightweight biomedical applications. J Mech Behav Biomed Mater 120:104603. https://doi.org/10.1016/j.jmbbm.2021.104603
16. Wang J-J, Tsai J-W, Su Y-C (2013) Piezoelectric rubber films for highly sensitive impact measurement. J Micromech Microeng 23(7):75009. https://doi.org/10.1088/0960-1317/23/7/075009
17. Qi Y, Jafferis NT, Lyons K Jr., Lee CM, Ahmad H, McAlpine MC (2010) Piezoelectric ribbons printed onto rubber for flexible energy conversion. Nano Lett 10(2):524–528. https://doi.org/10.1021/nl903377u
18. Ramadan KS, Sameoto D, Evoy S (2014) A review of piezoelectric polymers as functional materials for electromechanical transducers. Smart Mater Struct 23(3):033001. https://doi.org/10.1088/0964-1726/23/3/033001
19. Muralt P, Polcawich RG, Trolier-McKinstry S (2009) Piezoelectric thin films for sensors, actuators, and energy harvesting. MRS Bull 34(9):658–664. https://doi.org/10.1557/mrs2009.177
20. Mokhtari F, Azimi B, Salehi M, Hashemikia S, Danti S (2021) Recent advances of polymer-based piezoelectric composites for biomedical applications. J Mech Behav Biomed Mater 122:104669. https://doi.org/10.1016/j.jmbbm.2021.104669
21. Hu S, Shi Z, Zhao W, Wang L, Yang G (2019) Multifunctional piezoelectric elastomer composites for smart biomedical or wearable electronics. Compos B Eng 160:595–604. https://doi.org/10.1016/j.compositesb.2018.12.077
22. Wang X et al (2022) Highly stretchable lactate-based piezoelectric elastomer with high current density and fast self-healing behaviors. Nano Energy 97:107176. https://doi.org/10.1016/j.nanoen.2022.107176
23. Chou X et al (2018) All-in-one filler-elastomer-based high-performance stretchable piezoelectric nanogenerator for kinetic energy harvesting and self-powered motion monitoring. Nano Energy 53:550–558. https://doi.org/10.1016/j.nanoen.2018.09.006
24. Lee HB, Kim YW, Yoon J, Lee NK, Park S-H (2017) 3D customized and flexible tactile sensor using a piezoelectric nanofiber mat and sandwich-molded elastomer sheets. Smart Mater Struct 26(4):045032. https://doi.org/10.1088/1361-665X/aa64ca
25. Wang X et al (2023) A highly efficient piezoelectric elastomer with a green product cycle from fabrication to degradation. J Mater Sci 58(11):4840–4852. https://doi.org/10.1007/s10853-023-08349-y
26. Liu Y et al (2020) Electronic skin from high-throughput fabrication of intrinsically stretchable lead zirconate titanate elastomer. Research. https://doi.org/10.34133/2020/1085417

27. Qiu Y et al (2021) The frequency-response behaviour of flexible piezoelectric devices for detecting the magnitude and loading rate of stimuli. J Mater Chem C 9(2):584–594. https://doi.org/10.1039/D0TC02949A
28. Pan M et al (2021) Piezoelectric-driven self-sensing leaf-mimic actuator enabled by integration of a self-healing dielectric elastomer and a piezoelectric composite. Adv Intell Syst 3(8):2000248. https://doi.org/10.1002/aisy.202000248
29. Cafarelli A et al (2019) Small-caliber vascular grafts based on a piezoelectric nanocomposite elastomer: mechanical properties and biocompatibility. J Mech Behav Biomed Mater 97:138–148. https://doi.org/10.1016/j.jmbbm.2019.05.017
30. Mathew AT, Liu C, Ng TYN, Koh SJA (2019) A high energy dielectric-elastomer-amplified piezoelectric (DEAmP) to harvest low frequency motions. Sens Actuators A Phys 294:61–72. https://doi.org/10.1016/j.sna.2019.05.015
31. Cheng X, Gong Y, Liu Y, Wu Z, Hu X (2020) Flexible tactile sensors for dynamic triaxial force measurement based on piezoelectric elastomer. Smart Mater Struct 29(7):075007. https://doi.org/10.1088/1361-665X/ab8748
32. Seo J et al (2021) All-organic piezoelectric elastomer formed through the optimal cross-linking of semi-crystalline polyrotaxanes. Chem Eng J 426:130792. https://doi.org/10.1016/j.cej.2021.130792
33. Curry EJ et al (2018) Biodegradable piezoelectric force sensor. Proc Natl Acad Sci USA 115(5):909–914. https://doi.org/10.1073/pnas.1710874115
34. Roopaa TS, Narasimha Murthy HN, Praveen Kumar VV, Krishna M (2018) Development and characterization of PVDF thin films for pressure sensors. Mater Today: Proc 5(10):21082–21090. https://doi.org/10.1016/j.matpr.2018.06.503
35. Mamada S, Yaguchi N, Hansaka M, Yamato M, Yoshida H (2014) Performance improvement of piezoelectric-rubber by particle formation of linear aggregates. J Appl Polym Sci. https://doi.org/10.1002/app.39862
36. Fu R et al (2022) Intrinsically piezoelectric elastomer based on crosslinked polyacrylonitrile for soft electronics. Nano Energy 103:107784. https://doi.org/10.1016/j.nanoen.2022.107784
37. Nicolini L, Sorrentino A, Castagnetti D (2023) A soft piezoelectric elastomer with enhanced piezoelastic response. Smart Mater Struct. https://doi.org/10.1088/1361-665X/acef81
38. https://pubchem.ncbi.nlm.nih.gov/substance/24852494
39. https://www.dow.com/documents/en-us/productdatasheet/11/11-31/11-3184-sylgard-184-elastomer.pdf
40. Chen Y, Ye H, Wang X, Li Y, Yao X (2020) Grain size effects on the electric and mechanical properties of submicro BaTiO3 ceramics. J Eur Ceram Soc 40(2):391–400. https://doi.org/10.1016/j.jeurceramsoc.2019.09.033
41. https://www.stratasys.com/
42. https://www.femm.info/wiki/HomePage
43. https://www.mts.com/en/products/biomedical/biomaterial-test-systems/bionix-tabletop
44. https://markforged.com/materials/plastics/onyx
45. https://www.ni.com/en-ca/support/model.usb-6251.html
46. https://www.ni.com/en/shop/labview.html
47. Park CH (2001) On the circuit model of piezoceramics. J Intell Mater Syst Struct 12(7):515–522. https://doi.org/10.1177/104538901221453O2
48. https://www.freecad.org/
49. https://www.elmerfem.org/doxygen/index.html
50. L. Nicolini, A. Sorrentino, and D. Castagnetti, (2023) A Soft Free Shape Casted Piezoelectric Elastomer. In: 10th ECCOMAS Thematic Conference on Smart Structures and Materials, Patras: Dept. of Mechanical Engineering & Aeronautics University of Patras, pp 1722–1731 https://doi.org/10.7712/150123.9943.450540
51. https://classes.engineering.wustl.edu/2009/spring/mase5513/abaqus/docs/v6.6/books/usb/default.htm?startat=pt08ch28s02aus106.html
52. Liu T, Chen Y, Liu L, Liu Y, Leng J, Jin L (2021) Effect of imperfections on pseudo-bistability of viscoelastic domes. Extrem Mech Lett 49:101477. https://doi.org/10.1016/j.eml.2021.101477
53. https://classes.engineering.wustl.edu/2009/spring/mase5513/abaqus/docs/v6.6/books/key/default.htm?startat=ch18abk49.html
54. https://abaqus-docs.mit.edu/2017/English/SIMACAEANLRefMap/simaanl-c-steadystatetransport.htm
55. Gao X et al (2017) Improved electrical conductivity of PDMS/SCF composite sheets with bolting cloth prepared by a spatial confining forced network assembly method. RSC Adv 7(24):14761–14768. https://doi.org/10.1039/C7RA02061A

Authors and Affiliations

Lorenzo Nicolini[1] · Davide Castagnetti[1]

✉ Lorenzo Nicolini
lorenzo.nicolini@unimore.it

[1] Department of Sciences and Methods of Engineering, University of Modena and Reggio Emilia, Via G. Amendola 2, 42122 Reggio Emilia, Italy